

How reliable is the kinematical evidence for dark matter: the effects of non-sphericity, substructure and streaming motions

Teresa Sanchis¹, Ewa L. Łokas² and Gary A. Mamon^{3,4}

¹*Departament d’Astronomia i Meteorologia. Universitat de Barcelona, Avenida Diagonal 647, E-08028 Barcelona, Spain*

²*Nicolaus Copernicus Astronomical Center, Bartycka 18, 00-716 Warsaw, Poland*

³*Institut d’Astrophysique de Paris (CNRS UMR 7095), 98 bis Bd Arago, F-75014 Paris, France*

⁴*GEPI (CNRS UMR 8111), Observatoire de Paris, F-92195 Meudon, France*

24 June 2018

ABSTRACT

Using cosmological N -body simulations of dark matter haloes, we study the effects of non-sphericity, substructure and streaming motions in reproducing the structure and internal kinematics of clusters of galaxies from kinematical measurements. Fitting an NFW model to the 3D density profile, we determine the virial mass, concentration parameter and velocity anisotropy of the haloes, and then calculate the profiles of projected velocity moments, as they would be measured by a distant observer. Using these mock data, we apply a Jeans analysis for spherical objects to reproduce the line-of-sight velocity dispersion and kurtosis and fit the three parameters. We find that the line-of-sight velocity dispersion and kurtosis profiles of a given halo can vary considerably with the angle of view of the observer. We show that the virial mass, concentration parameter and velocity anisotropy of the haloes can be reproduced satisfactorily independently of the halo shape, although the virial mass tends to be underestimated, the concentration parameter overestimated, while the recovered anisotropy is typically more tangential than the true one. The mass, concentration and velocity anisotropy of haloes are recovered with better precision when their mean velocity profiles are near zero.

Key words: methods: N -body simulations – methods: analytical – galaxies: clusters: general – galaxies: kinematics and dynamics – cosmology: dark matter

1 INTRODUCTION

There is a long tradition of determining the internal kinematical properties of bound systems based on the Jeans equations, which are velocity moments of the collisionless Boltzmann equation, and which link the 3D velocity moments (e.g. velocity dispersion and kurtosis) to the potential gradient. The Jeans equations are thus used to model the mass and velocity distribution inside elliptical galaxies (e.g. Binney & Mamon 1982), clusters of galaxies (e.g. Kent & Gunn 1982; Merritt 1987), as well as globular clusters (e.g. Merrifield & Kent 1990). The standard Jeans approach for the determination of the mass and velocity distribution assumes equilibrium and sphericity of the system. However, even in the inner parts of an object, there is non-virialized matter, for example matter falling into a cluster for the first time or smaller clumps in the process of relaxation. Such non-virialized matter could produce misleading results when a cluster is studied through a Jeans analysis. Moreover,

clusters of galaxies are not observed to be spherically symmetric (Binggeli 1982; Wang & Ulmer 1997), nor are simulated structures of dark matter particles with the masses of clusters of galaxies (Cole & Lacey 1996; Jing & Suto 2002).

One way to avoid non-virialized matter within a cluster is to restrict the Jeans analysis to the population of elliptical galaxies, which is thought to be dynamically relaxed (Tully & Shaya 1984; Biviano et al. 2003; Łokas & Mamon 2003). The question of how the existing substructure and non-sphericity may affect the results can only be fully addressed by cosmological N -body simulations including realistic galaxy formation, where all 3-dimensional information would be available.

The effect of incomplete virialization of structures of dark matter particles seen in cosmological N -body simulations on the estimates of the mass of a single cluster through the Jeans equation has been addressed by Tormen, Bouchet & White (1997). They showed that even for significantly perturbed haloes, the mass $M(r)$ at dis-

tances larger than 2% of the virial radius inferred by the proper Jeans analysis is within 30% (r.m.s.) of the true mass and departs from it by less than 20% (r.m.s.) for average or relaxed haloes.

In this work, we use cosmological N -body simulations and analytical modelling to study the effect of departures from equilibrium and non-sphericity of dark matter haloes on the inferred properties of the halo and velocity distribution of its particles. We measure the mass and velocity distribution in the haloes and calculate the projected velocity moments as an observer would do. We then perform a kinematic analysis based on the Jeans equations to check to what extent we can reproduce the properties of the haloes from the second-order (line-of-sight velocity dispersion) and fourth-order (line-of-sight kurtosis) velocity moments.

The paper is organized as follows. In Section 2, we describe the N -body simulations used and calculate the properties of the haloes chosen for analysis. In Section 3, we estimate projected velocity moments of the haloes. Section 4 is devoted to analytical modelling of those moments based on Jeans formalism and testing its reliability in reproducing the properties of the haloes. The discussion follows in Section 5.

2 THE SIMULATED DARK MATTER HALOES

We have used the N -body simulations carried out by Hatton et al. (2003) with their **GalICS** hybrid N -body/semi-analytic model of hierarchical galaxy formation. The description of this model can be found in Hatton et al. (2003). The N -body simulation contains 256^3 particles of mass $8.272 \times 10^9 M_\odot$ in a box of size 150 Mpc and its softening length amounts to spatial resolution of 29 kpc. The simulation was run for a flat universe with cosmological parameters $\Omega_0 = 0.333$, $\Omega_\Lambda = 0.667$, $H_0 = 66.7 \text{ km s}^{-1} \text{ Mpc}^{-1}$, and $\sigma_8 = 0.88$. Once the simulation is run, haloes of dark matter are detected with a ‘friends-of-friends’ (FOF) algorithm (Davis et al. 1985) using a variable linking length such that the minimum mass of the FOF groups is $1.65 \times 10^{11} M_\odot$ (20 particles) at any time step. With this method, over 2×10^4 haloes are detected at the final timestep, corresponding to the present-day ($z = 0$) Universe.

We restrict our analysis to dark matter particles. Although the **GalICS** simulations we use include galaxy formation and evolution, this part of the simulations is based on a semi-analytical approach, which for our purposes is not yet satisfactory. For example, the isotropic velocity distribution of **GalICS** galaxies is imposed and is not a result of virialization. We therefore conclude that the galaxies in these simulations are not reliable tracers of the overall dynamical properties of the haloes and cannot be used to infer the density and velocity distributions from the ‘observed’ velocity moments.

For our analysis, we have chosen the ten most massive haloes formed in the simulation box (labelled hereafter in order of decreasing virial mass as halo 1, halo 2 and so forth). We estimated their virial radii, r_{100} , as the distances from the centre where the mean density is 100 times the present critical density (in agreement with the so-called spherical collapse model, see Kitayama & Suto 1996; Lokas & Hoffman 2001). The centres of the haloes are determined as the local density maxima which turn out to be

Table 1. Three-dimensional properties of the simulated haloes

| Halo | Axis ratio | M_{100} ($10^{14} M_\odot$) | r_{100} (Mpc) | c | $\langle\beta\rangle$ | \bar{v}_r (v_{100}) |
|------|---------------|------------------------------------|--------------------|------|-----------------------|------------------------------|
| 1 | 2.3 : 1.3 : 1 | 16.7 | 3.2 | 5.6 | 0.40 ± 0.06 | 0.005 |
| 2 | 1.9 : 1.1 : 1 | 8.5 | 2.5 | 5.0 | 0.13 ± 0.03 | 0.103 |
| 3 | 2.8 : 2.0 : 1 | 8.1 | 2.5 | 4.5 | 0.24 ± 0.05 | 0.134 |
| 4 | 3.3 : 1.3 : 1 | 7.0 | 2.4 | 7.1 | 0.14 ± 0.06 | -0.260 |
| 5 | 2.0 : 2.0 : 1 | 4.5 | 2.1 | 7.9 | 0.15 ± 0.07 | 0.065 |
| 6 | 2.6 : 1.4 : 1 | 4.3 | 2.0 | 5.0 | 0.36 ± 0.05 | 0.028 |
| 7 | 1.8 : 1.4 : 1 | 4.1 | 2.0 | 8.9 | -0.03 ± 0.05 | -0.079 |
| 8 | 2.4 : 1.6 : 1 | 3.9 | 2.0 | 10.0 | 0.44 ± 0.03 | -0.018 |
| 9 | 2.2 : 1.5 : 1 | 3.2 | 1.8 | 7.1 | 0.08 ± 0.12 | -0.012 |
| 10 | 1.8 : 1.3 : 1 | 2.9 | 1.8 | 10.0 | -0.23 ± 0.08 | -0.168 |

slightly different than the centres of mass found using the FOF algorithm. Within the virial radius, the haloes have 2×10^5 particles for the most massive halo and 4×10^4 particles for the least massive one of the haloes we have chosen. The masses of the haloes, $M_{100} = M(r_{100})$, are listed in Table 1.

All haloes have similar 3D radial phase space distributions. An example of such a distribution for the most massive halo is presented in Figure 1. The Figure shows the radial velocity (with respect to the centre of the halo) of the particles in units of the circular velocity at r_{100} ($v_{100} = v_c(r_{100}) = \sqrt{GM_{100}/r_{100}}$) as a function of radial distance measured in units of r_{100} . We have divided the phase space into different regions corresponding to different dynamical states that we expect to find in a typical dark matter halo. Inside the virial radius, we can identify three regions. The region with low to moderate absolute velocities is likely to be populated by virialized particles, although there are indications of a group of particles at $r = 0.3r_{100}$ slowly moving into the halo core. On the outskirts of the velocity distribution we can find particles whose dynamical state is not clear, as they could be either high-velocity outliers of the virialized component or else infalling towards the cluster core or already in a rebound regime after a passage through the centre. Beyond the virial radius, we can also find particles in a rebound trajectory and particles on the infalling branch (which includes particles expanding away from the cluster beyond the turnaround radius at 2.5–4 virial radii). In Figure 1, these five different subsamples are denoted by **virialized**, **rebound**, **infall**, **vir-inf?** and **vir-reb?**, respectively, where the question marks indicate the uncertainty in the actual dynamical state of these subsamples.

It is important to note that when studying projected quantities we need to consider all five subsamples, as well as the whole sample (which will be marked hereafter by ‘all’), because, as seen projected on the sky, there are particles belonging to each subsample that fall inside the ‘virial’ cylinder whose projected radius is the virial radius r_{100} , but there is no way of determining which of these particles are actually within the ‘virial’ sphere of radius r_{100} (inscribed in the virial cylinder).

Figure 2 shows the density distribution in the most massive halo 1 as a function of radial distance in units of r_{100} .

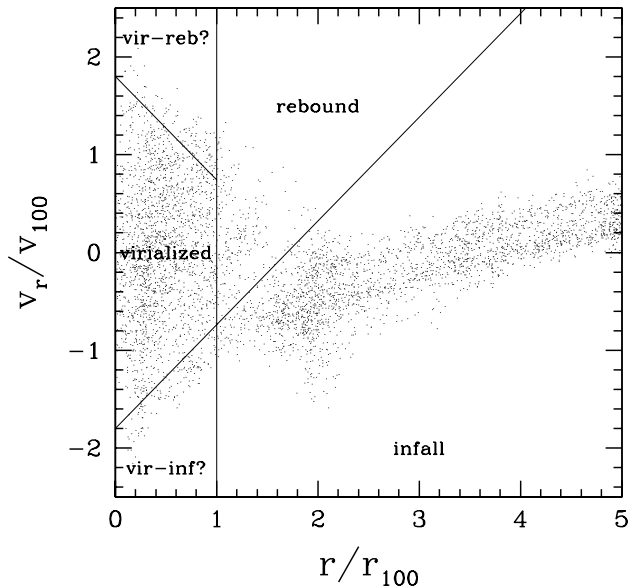


Figure 1. 3D radial phase space diagram (radial velocity, Hubble flow included, versus radial distance, both with respect to the cluster centre and normalized to virial quantities v_{100} and r_{100} , respectively) for a random set of 1% of particles of the most massive of the simulated haloes (halo 1). The oblique lines separating the dynamical regimes were drawn ‘by eye’ and correspond to $v_r/v_{100} = 1.8 - 1.06 r/r_{100}$ (bottom) and $v_r/v_{100} = -1.8 + 1.06 r/r_{100}$ (top).

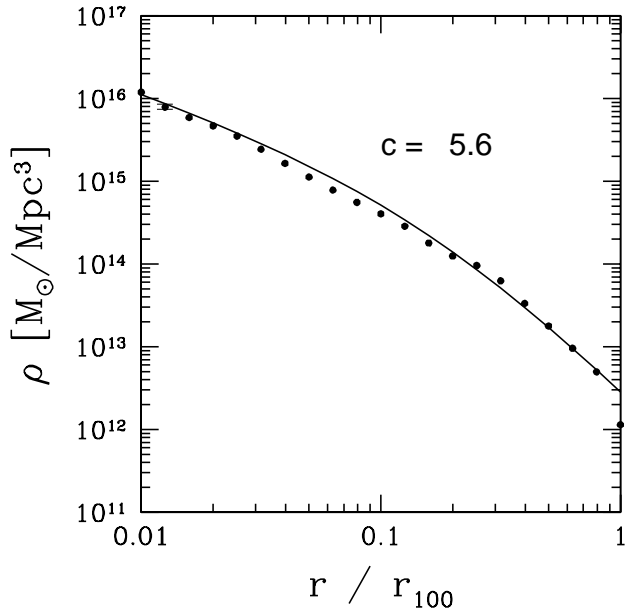


Figure 2. Density profile of halo 1. The measurements were done in radial bins of equal logarithmic length and errors were estimated as Poisson fluctuations. The error bar in the second point shows the maximum error assigned to measurements. The curve is the best-fitting NFW profile with concentration $c = 5.6$.

We found that the measured density profile is well approximated by the NFW formula (Navarro, Frenk & White 1997)

$$\frac{\rho(s)}{\rho_{c,0}} = \frac{\Delta_c c^2 g(c)}{3 s (1 + cs)^2}, \quad (1)$$

where $s = r/r_{100}$, $\rho_{c,0}$ is the present critical density, $\Delta_c = 100$, c is the concentration parameter and $g(c) = [\ln(1+c) - c/(1+c)]^{-1}$. The statistical errors are much smaller than the departures due to substructure in the halo, but the overall fit is satisfactory. We find that the best-fitting concentration parameter for halo 1 is $c = 5.6$. The virial mass of halo 1 is $M_{100} = 1.67 \times 10^{15} M_\odot$ so the concentration we estimated is consistent with the dependence of c on mass inferred from N -body simulations by Bullock et al. (2001), also run with a Λ CDM cosmology. Similar results are obtained for other haloes. The fitted parameters are summarized in Table 1.

In Figure 3 we present radial profiles of the mean radial velocity in units of the circular velocity at r_{100} and the anisotropy parameter

$$\beta = 1 - \frac{\sigma_\theta^2(r)}{\sigma_r^2(r)} \quad (2)$$

for the ten haloes, where σ_θ and σ_r are the velocity dispersions (with respect to the mean velocities) discussed in detail in the next Sections. We show measurements for all particles inside the sphere of radius r_{100} . The curves represent the anisotropy or mean radial velocity of dark matter particles enclosed in shells of thickness $0.1r_{100}$ centered at $0.05r_{100}$, $0.15r_{100}$ etc. As we can see, the orbits of most of the haloes are mildly radial, with positive mean β . We have calculated the unweighted mean anisotropy inside the virial radius. These values are listed in Table 1, where the uncertainties are the dispersions of the values about the unweighted mean. The anisotropy does not vary strongly with radius so in the modelling which follows we will assume it to be constant and equal to the mean value inside the virial radius. However, it is interesting to note that the variation of β with distance from the centre is very different for each of the analyzed haloes. As for the mean radial velocity, we can see from Figure 3 that it is consistent on average with zero inside r_{100} for most haloes, albeit with non-negligible radial variations caused by internal streaming motions, including some abrupt variations suggesting the presence of smaller haloes (akin to groups of galaxies) falling in or bouncing out of the halo. In Table 1 we list this quantity in units of v_{100} . The negative sign indicates infall motion towards the centre of the halo.

Since we wish to study the effect of non-sphericity of haloes by choosing different directions of observation, we have determined the principal axes of our haloes from their moments of inertia, using particles at radial distances up to r_{100} . The ratios of the eigenvalues of the inertia tensor, listed in Table 1, show significant departures from sphericity.

3 VELOCITY MOMENTS OF DARK MATTER PARTICLES

We now study the kinematical properties of haloes as they would be seen by a distant observer. The quantities discussed are all projected along the line of sight. With the

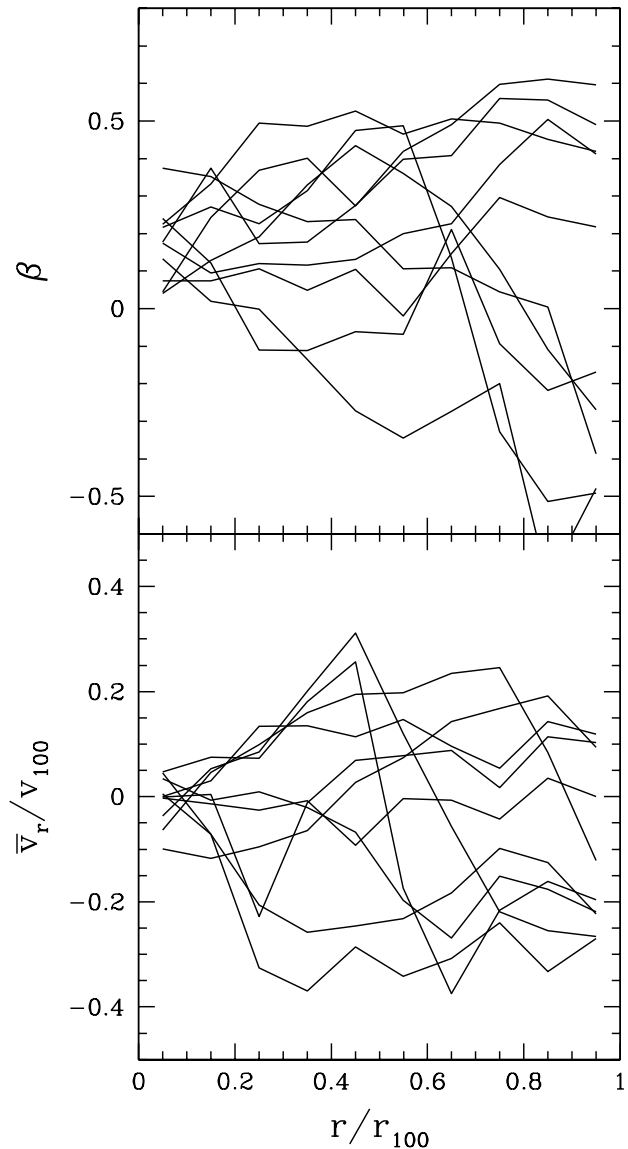


Figure 3. The radial profile of the anisotropy parameter β (*top panel*) and the mean radial velocity in units of the circular velocity at r_{100} (*bottom panel*) for all particles inside r_{100} for the 10 haloes of Table 1.

Jeans formalism, we can only model the projected velocity moments of objects in equilibrium, and thus we cannot make any prediction about the velocity moments of the regions of phase space called ‘rebound’, ‘infall’, ‘vir-reb?’ and ‘vir-inf?’ in Figure 1. Moreover, not all particles inside r_{100} are virialized, as they could be falling into the core for the first time or be on a rebound orbit not yet in equilibrium. However, the division of the phase space into the 5 regions (Fig. 1) was made by eye, with no exact determination of the dynamical state of the particles, and it was only based on the radial component of the particle velocities. This could produce misleading results in the analysis of the velocity moments, which involve all components of the velocity. For these reasons, in what follows, we will restrict ourselves to the study of the velocity moments of all particles inside the virial sphere of radius r_{100} and all particles within the virial

cylinder of projected radius smaller than r_{100} . The latter would be the ones used in the Jeans formalism by an observer unable to distinguish which particles actually lie in the virial sphere of radius r_{100} .

We mimic the observations as follows. For each halo, we place an observer at either 0° , 45° or 90° with respect to the major axis (see Table 1) so that the three chosen directions are in the same plane defined by the major axis and the sum of the other two axes. The choice of axes is dictated by the non-sphericity of the set of particles within the virial sphere, but also of the filaments of groups and other matter falling into the virial sphere out to scales $\simeq 10 r_{100}$. It turns out that the principal axes on scales of $\simeq 10 r_{100}$ are very similar to those computed for $r < r_{100}$, so we restrict ourselves to the principal axes obtained from the tensor of inertia of the particles within the virial sphere. We then project all the particle velocities along the line of sight and the distances on the surface of the sky. In Figure 4, we show line-of-sight velocities of dark matter particles in halo 1 projected along the major axis as a function of projected distance from the centre in units of r_{100} .

Observers remove a fraction of the interlopers of a cluster by excluding the high-velocity outliers. Here, we remove the high-velocity outliers from our mock samples in a similar way as done by Kent & Gunn (1982) and Lokas & Mamon (2003) for clusters of galaxies. The velocity cuts are shown as solid curves in Figure 4. Less than 2% of all particles within the virial cylinder were removed in this fashion. Although the main body of the halo is quite well defined in velocity space, with much more particles than there are galaxies in a cluster, the gaps between the halo and the background are not as visible as found by Lokas & Mamon (2003) for the Coma cluster. After applying this selection procedure, the fraction of particles lying inside the cylinder of projected radius r_{100} that are actually outside the sphere of radius r_{100} is between 6% and 35%, with a mean of 15%.

We divide the projected radius in ten bins and calculate, in each bin of projected radius, the mean, dispersion, skewness, and kurtosis of the line-of-sight velocities, v_i , according to the following formulae

$$\bar{v}_{\text{los}} = \frac{1}{N} \sum_{i=1}^N v_i \quad (3)$$

$$\sigma_{\text{los}}^2 = \frac{1}{N-1} \sum_{i=1}^N (v_i - \bar{v}_{\text{los}})^2 \quad (4)$$

$$s_{\text{los}} = \frac{1}{N} \sum_{i=1}^N \left(\frac{v_i - \bar{v}_{\text{los}}}{\sigma_{\text{los}}} \right)^3 \quad (5)$$

$$\kappa_{\text{los}} = \frac{1}{N} \sum_{i=1}^N \left(\frac{v_i - \bar{v}_{\text{los}}}{\sigma_{\text{los}}} \right)^4 - 3 \quad (6)$$

where N represents the number of particles per bin.

To see the effects of non-sphericity, we show the results for haloes 1, 4 and 5, which have three different shapes: halo 5 is oblate, halo 4 is roughly prolate and halo 1 is tri-axial. The results for halo 1 are shown in Figures 5–7 for observers situated at 0° , 45° and 90° with respect to the major axis. The errors were estimated using bootstraps, but since the number of particles in each bin is very large (of

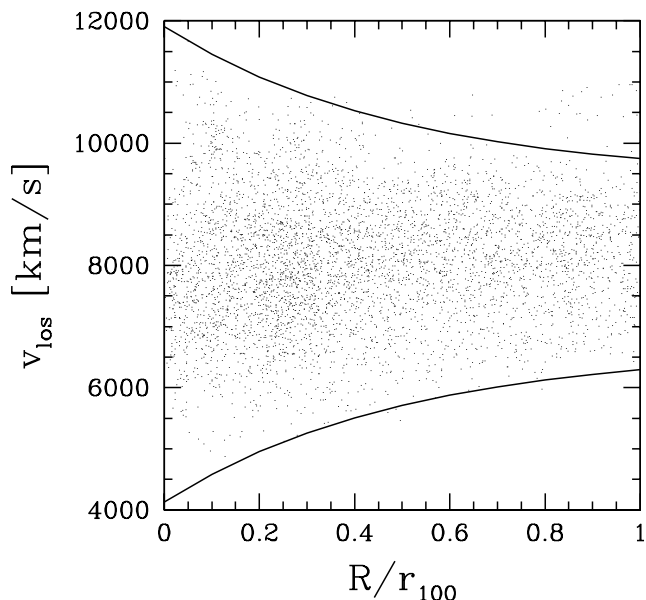


Figure 4. Line-of-sight velocities of a random set of 2% of the dark matter particles in halo 1 projected along the major axis as a function of projected distance from the centre in units of r_{100} . The *curves* indicate the cuts used to distinguish between particles belonging to the halo from the background. The vertical clumps indicate groups of particles (nearly all within the virial sphere).

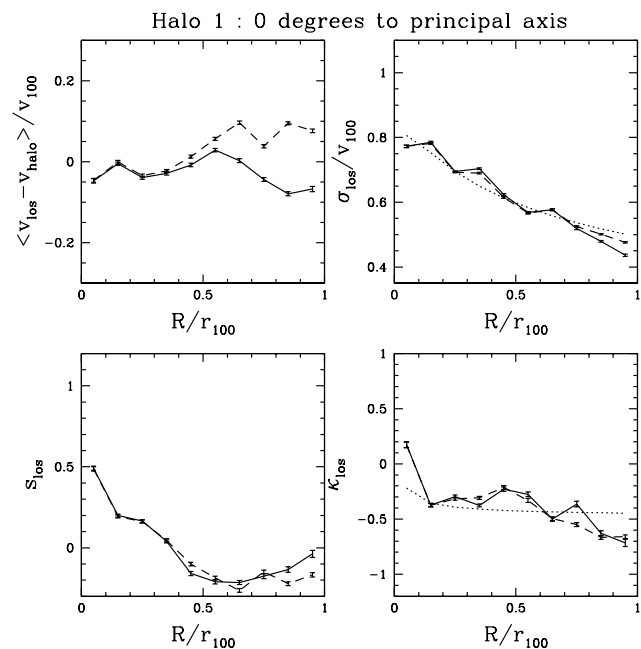


Figure 5. Projected velocity moments of the dark matter particles in halo 1 measured at 0° to the principal axis. The *upper left panel* shows the mean line-of-sight velocity with respect to the velocity of the centre of the halo in units of the circular velocity at r_{100} . The *upper right panel* gives the line-of-sight velocity dispersion in the same units. The two *lower panels* give the skewness (*left*) and kurtosis (*right*). In each panel the *solid line* shows results for particles lying inside the sphere of radius r_{100} , while the *dashed line* is for all particles. The *dotted curve* shows the fits obtained from the Jeans equations.

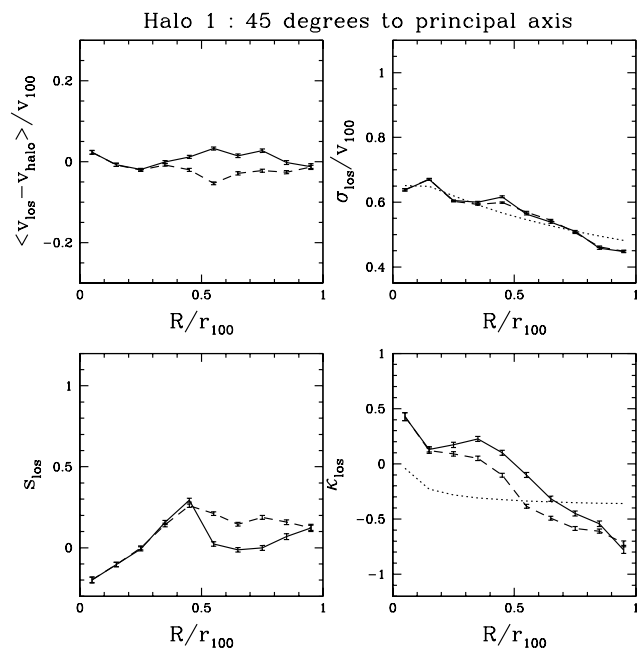


Figure 6. Same as Figure 5, but measured at 45° to the principal axis.

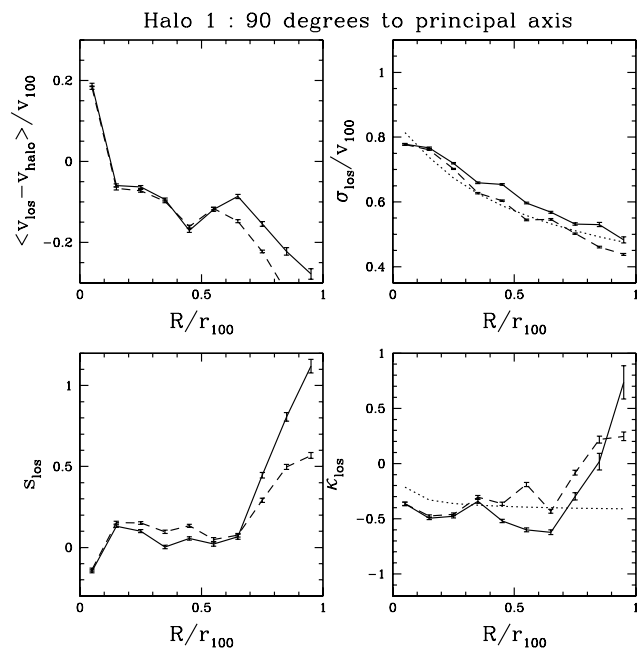


Figure 7. Same as Figure 5, but measured at 90° to the principal axis.

the order of 10^4), the errors are small and do not account for the variability of the profiles, which is mainly due to substructure. In each panel, the dashed line shows results for all particles that in projection end up with a projected radius smaller than the virial radius, whether or not they are actually within the virial radius in 3D space. The solid line shows results for the particles really lying inside r_{100} . In the right-hand panels presenting even moments (velocity dispersion and kurtosis) in Figures 5–7 we also show dotted

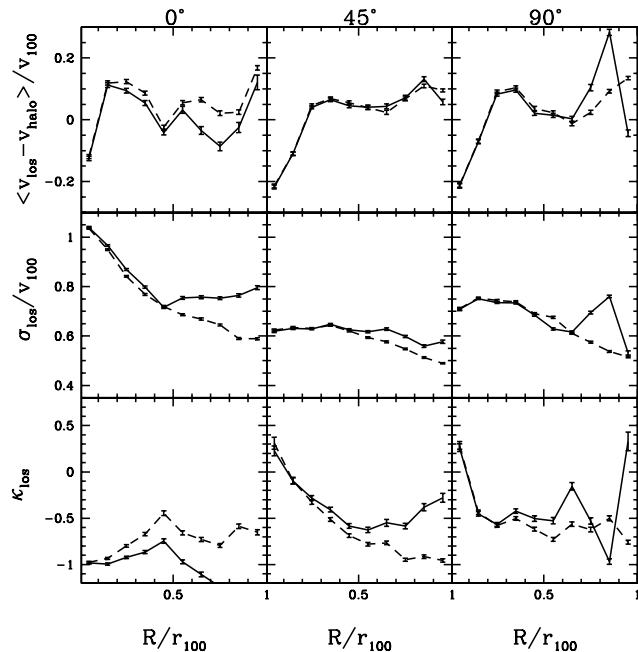


Figure 8. Same as Figures 5-7 but for halo 4. Line-of-sight skewness is not plotted. No theoretical predictions are shown.

lines resulting from the fitting procedure based on the Jeans formalism presented in Section 4.

The variation of the mean velocity with projected radius provides an indication of the amount of substructure present in the halo. For observers at 0° and 45° with respect to the major axis of halo 1, the mean velocity with respect to the centre of the halo is approximately zero for every radial bin, indicating, if not the lack of substructure, at least the compensation of effects of different substructures. This is true for the two subsets of particles studied, especially for particles actually within the virial sphere. For an observer at 90° with respect to the major axis of halo 1, we find a departure of the mean velocity from the velocity of the centre of the halo, which indicates the presence of substructure. As could be expected, this radial variation of the mean velocity is more pronounced for the particles we find in projection inside r_{100} that are not necessarily within the virial sphere of radius r_{100} .

Contrary to the case of elliptical galaxies, where velocity moments are measured from spectra obtained in slits, e.g. along the major axis, and thus do not involve averaging in shells of similar projected radius, here and in the analysis of galaxy motions in clusters the mean projected velocity is less affected by the presence of global motions like rotation or infall. Therefore, the estimation of the bulk velocities requires the 3D information. We find that the mean velocities in the radial and tangential directions inside the virial radius are typically of the order of few percent of v_{100} , except for halo 4 and halo 10 where significant net radial infall seems to be present (see Table 1).

Figures 8 and 9 illustrate how the velocity moments depend on the shape of the given halo. To save space, we only show the even moments that we will model in the next Section and the mean line-of-sight velocity with respect to the velocity of the centre to test the relaxation of the haloes.

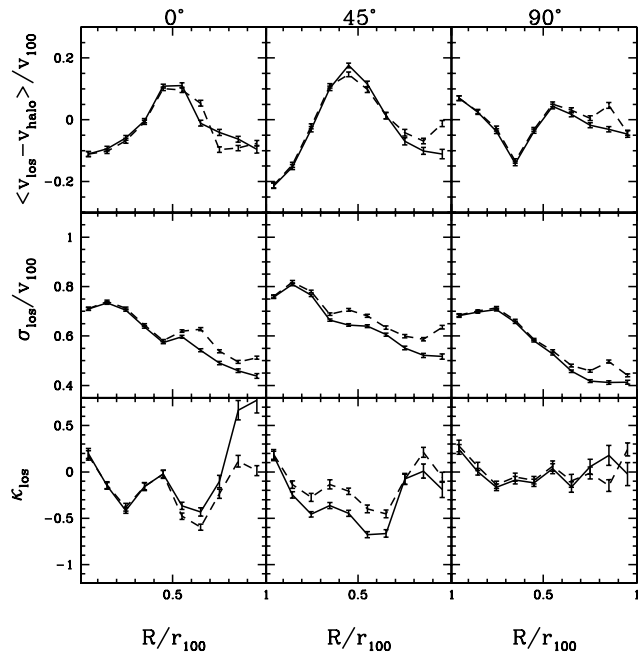


Figure 9. Same as Figure 8, but for halo 5.

For the sake of clarity of the plots, we do not show the fits based on the Jeans equations, although we will discuss them in the following section.

Even with significant noise from substructure, such as the trend for high mean velocity at $R \simeq 0.5r_{100}$ for halo 5 (Fig. 9) probably arising from a group bouncing out of the halo, we can see some common trends in Figures 5–9. First, the line-of-sight velocity dispersion and kurtosis profiles can differ substantially for a given halo seen along three different axes (especially in halo 4). Moreover, the velocity moments are not strongly affected by the presence of particles outside the virial radius, i.e. the solid and dashed lines typically do not differ significantly. This is understandable as the virial sample is a subsample of the ‘all’ sample and the mean difference in the number of particles is less than 20% as previously noted. The discrepancies between the velocity moments are more important for larger projected distances from the centre of a halo, as the surface density of the 3D haloes decreases faster than that of the surrounding material.

4 MODELLING OF THE VELOCITY MOMENTS

We now briefly describe the Jeans formalism for modelling the projected velocity moments of virialized objects and apply it to recover the properties of the haloes. The detailed description of the calculations involved can be found in Lokas (2002) and Lokas & Mamon (2003) (see also Merrifield & Kent 1990; van der Marel et al. 2000).

Our purpose here is to reproduce the projected velocity moments discussed in the previous Section by solving the Jeans equations for the second and fourth velocity moments and adjusting the parameters describing the mass and velocity distribution in the haloes. We will then verify whether

the fitted parameters match the real properties of the haloes. The Jeans analysis assumes that the system is spherically symmetric and in equilibrium, that there are no net streaming motions (no infall and no rotation) so that the odd velocity moments vanish. As we have seen in the previous Section, none of these is exactly the case for dark matter haloes. We want to check to what extent violating these assumptions affects the recovered properties of the haloes.

One difference with respect to the analysis of galaxies is that the dark matter particles are very numerous in our simulations (of order 10^5 per halo) while the number of galaxies in a cluster usually does not exceed a thousand. This is the reason why the errors due to substructure will be more significant here than sampling errors which are the dominant ones in measured velocity moments of galaxies.

The second order velocity moments are $\overline{v_r^2}$ and $\overline{v_\theta^2} = \overline{v_\phi^2}$ and we will denote them hereafter by σ_r^2 and σ_θ^2 respectively. They can be calculated from the lowest order Jeans equation (e.g. Binney & Mamon 1982)

$$\frac{d}{dr}(\nu\sigma_r^2) + \frac{2\beta}{r}\nu\sigma_r^2 = -\nu\frac{d\Phi}{dr}, \quad (7)$$

where ν is the 3D density distribution of the tracer population and Φ is the gravitational potential. Since in our case dark matter particles trace their own gravitational potential, we have $\nu(r) = \varrho(r)$. We assume that the dark matter distribution is given by the NFW profile (1) characterized by its virial mass M_{100} and concentration c . We solve equation (7) assuming the anisotropy parameter of equation (2) to be constant with $-\infty < \beta \leq 1$. This model covers all interesting possibilities from radial orbits ($\beta = 1$) to isotropy ($\beta = 0$) and circular orbits ($\beta \rightarrow -\infty$).

The solution of the lowest order Jeans equation with the boundary condition $\sigma_r \rightarrow 0$ at $r \rightarrow \infty$ for $\beta = \text{const}$ is (e.g. Lokas & Mamon 2003)

$$\nu\sigma_r^2(\beta = \text{const}) = r^{-2\beta} \int_r^\infty r^{2\beta} \nu \frac{d\Phi}{dr} dr. \quad (8)$$

As discussed in the previous Section, the quantity an observer would measure is the line-of-sight velocity dispersion obtained from the 3D velocity dispersion by integrating along the line of sight (Binney & Mamon 1982)

$$\sigma_{\text{los}}^2(R) = \frac{2}{I(R)} \int_R^\infty \left(1 - \beta \frac{R^2}{r^2}\right) \frac{\nu\sigma_r^2 r}{\sqrt{r^2 - R^2}} dr, \quad (9)$$

where $I(R)$ is the surface distribution of the tracer and R is the projected radius. In our case $I(R)$ is given by the projection of the NFW profile (see Lokas & Mamon 2001). Introducing equation (8) into equation (9) and inverting the order of integration, the calculation of σ_{los} can be reduced to one-dimensional numerical integration of a formula involving special functions for arbitrary $\beta = \text{const}$.

It has been established that systems with different densities and velocity anisotropies can produce identical $\sigma_{\text{los}}(R)$ profiles (see e.g. Merrifield & Kent 1990; Merritt 1987). This degeneracy can be partially lifted through the modelling of the fourth-order moment. With $\beta = \text{const}$, the solution of the Jeans equation for the fourth-order moment

$$\frac{d}{dr}(\nu\overline{v_r^4}) + \frac{2\beta}{r}\nu\overline{v_r^4} + 3\nu\sigma_r^2\frac{d\Phi}{dr} = 0, \quad (10)$$

is (see Lokas 2002; Lokas & Mamon 2003)

$$\overline{v_r^4}(\beta = \text{const}) = 3r^{-2\beta} \int_r^\infty r^{2\beta} \nu\sigma_r^2(r) \frac{d\Phi}{dr} dr. \quad (11)$$

By projection, we obtain the line-of-sight fourth moment

$$\overline{v_{\text{los}}^4}(R) = \frac{2}{I(R)} \int_R^\infty \frac{\nu\overline{v_r^4} r}{\sqrt{r^2 - R^2}} g(r, R, \beta) dr, \quad (12)$$

where $g(r, R, \beta) = 1 - 2\beta R^2/r^2 + \beta(1 + \beta)R^4/(2r^4)$.

Introducing equations (8) and (11) into (12) and inverting the order of integration, the calculation can be reduced to a double integral. In the following, we use the fourth projected moment scaled with σ_{los}^4 in the form of projected kurtosis

$$\kappa_{\text{los}}(R) = \frac{\overline{v_{\text{los}}^4}(R)}{\sigma_{\text{los}}^4(R)} - 3, \quad (13)$$

where the value of $\kappa_{\text{los}}(R) = 3$ valid for a Gaussian distribution has been subtracted.

We can now calculate the predictions of equations (9) and (12) for a given mass distribution and velocity anisotropy β . As already discussed, we assume that the mass is given by the NFW distribution. For halo 1 we found the concentration of $c = 5.6$. For this value and different β we obtain the profiles of $\sigma_{\text{los}}(R)$ and $\kappa_{\text{los}}(R)$ shown in Figure 10. The values of σ_{los} are expressed in units of v_{100} and distances are in units of r_{100} . With these scalings, the predictions do not explicitly depend on the mass of the halo. The lines show results for different values of $\beta = -0.3, 0, 0.3, 0.6$ and 0.9 , as indicated.

We see that for increasingly radial orbits (increasing β), the profile of σ_{los} turns steeper (e.g. Tonry 1983). Moreover, the kurtosis profile becomes more convex for increasingly radial orbits as opposed to the concave shapes in the case of isotropic and circular orbits. Since our measured kurtosis profiles in the previous Section have a concave shape and are slightly negative we do not expect the orbits to depart significantly from isotropic, which is consistent with the measured anisotropy parameter (see Table 1).

Mimicking the procedure used by observers to infer the mass and anisotropy profiles of galaxies and clusters, we fit the measured profiles of σ_{los} and κ_{los} of the ten haloes by solving equations (9) and (12) and adjusting the parameters M_{100} , c and β , assuming that the objects are spherical and that their dark matter distribution is given by the NFW density profile. The fit is done by minimizing χ^2 for the 20 ‘data points’ of σ_{los} and κ_{los} together (the data points are independent because the number of particles in each radial bin is very large, see the discussion in the Appendix of Lokas & Mamon 2003). The data points were weighted by the assigned bootstrap errors although they do not account for the real variability of the data and therefore the quality of the fits in terms of χ^2 is very bad. The best-fitting velocity moments found for halo 1 are shown as dotted lines in Figures 5–7.

In reality, when dealing with real galaxy data for clusters, the bins would include a few tens of objects instead of thousands, resulting in errors larger by at least an order of magnitude. To see how the sampling errors affect the determination of the dynamical parameters of clusters, we have also measured for each halo the velocity moments for a set of 40 randomly chosen particles per distance bin. This number of particles is chosen to be similar to the usual num-

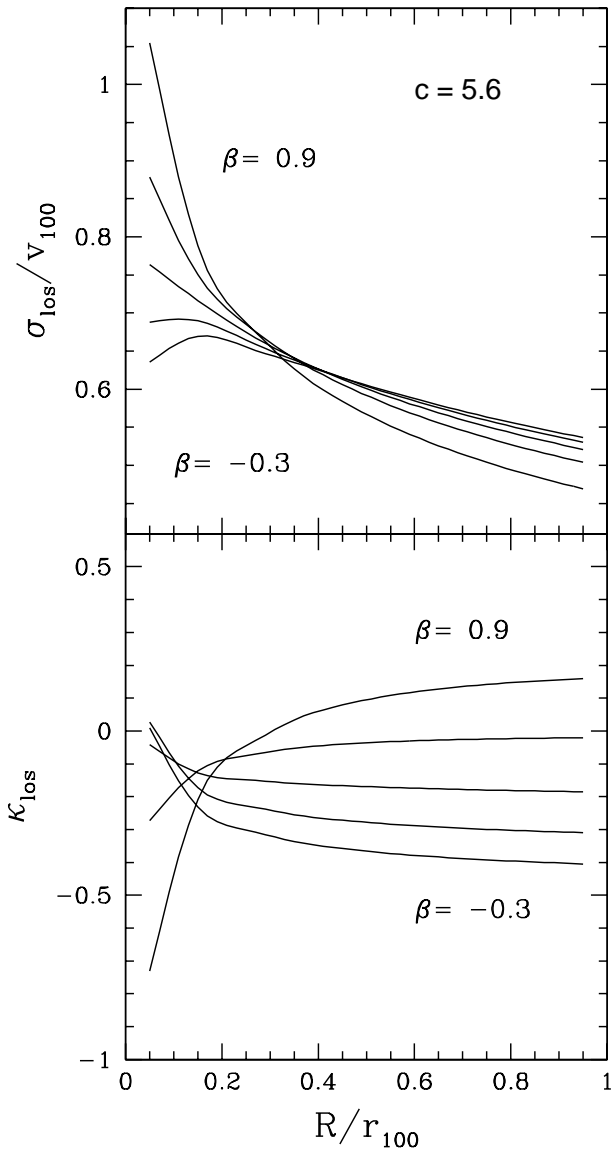


Figure 10. Predicted profiles of $\sigma_{\text{los}}(R)$ and $\kappa_{\text{los}}(R)$ for dark matter halo with concentration $c = 5.6$ and different values of $\beta = -0.3, 0, 0.3, 0.6$ and 0.9 . The values of σ_{los} are scaled with circular velocity at r_{100} and distances are in units of r_{100} . These theoretical profiles are independent of the virial mass M_{100} .

ber of galaxies used in real clusters e.g. by Lokas & Mamon (2003). Errors were assigned as described in the Appendix of Lokas & Mamon (2003). We have then performed the same fitting procedure as described above.

The best-fitting parameters for the haloes estimated with all dark matter particles are shown in the left column of Figure 11 as different symbols depending on the direction of observation with respect to the major axis: 0° (circles), 45° (triangles) and 90° (squares). The crosses mark the ‘real’ values of the parameters listed in Table 1. In the right column of Figure 11, we show the best-fitting parameters estimated with 400 particles (40 particles per bin).

Due to a rather time-consuming integration involved in the calculation of kurtosis, we restricted our analysis

Table 2. Results of the fitting procedure

| Particles per bin | $\Delta \log M_{100}$ | | $\Delta \log c$ | | $\Delta \beta$ | | $\Delta \log(\sigma_r/\sigma_\theta)$ | |
|----------------------|-----------------------|----------|-----------------|----------|----------------|----------|---------------------------------------|----------|
| | mean | σ | mean | σ | mean | σ | mean | σ |
| All | -0.03 | 0.09 | 0.20 | 0.18 | -0.78 | 1.04 | -0.12 | 0.12 |
| 40 | -0.07 | 0.10 | 0.08 | 0.24 | -0.20 | 0.48 | -0.04 | 0.11 |

to the ten most massive haloes. The general conclusion is that when taking into account all three fitting parameters, for all haloes their best-fitting virial mass M_{100} is reasonably well recovered: the discrepancy between the best-fitting value and the real M_{100} (measured using 3D information) is smaller than 62% (this large discrepancy is obtained for halo 10 when observed at 45° with respect to the major axis). The next biggest error was obtained for halo 5 (37% when observed at 45° with respect to the major axis).

In the case of the two remaining parameters, concentration c and anisotropy β , all haloes show common trend in the discrepancies: β is underestimated while c overestimated, especially for the fitting including all dark matter particles. The discrepancies can be traced to the specific behaviour of the σ_{los} and κ_{los} profiles. For example, in the case of halo 1 the three kurtosis profiles (see Figures 5-7) give similar β values, however the σ_{los} is much shallower for the observation angle of 45° than in the two remaining cases. As already mentioned, κ_{los} is mainly sensitive to the velocity anisotropy. Since the line-of-sight velocity dispersion profile can be made steeper in the centre either with a steeper density profile or with more radial orbits, and since the anisotropy parameter is almost the same in all three directions, we can expect the inferred concentration to be somewhat lower for the 45° direction, which is indeed the case. The situation is similar for halo 4. The kurtosis forces the anisotropy to be very tangential, so the very steep σ_{los} profile at 0° (the leftmost middle panel of Figure 8) requires a very large concentration of the density profile.

We have calculated the means and standard deviations of the differences between the fitted parameters ($\log M_{100}$, $\log c$, and β or $\log \sigma_r/\sigma_\theta$) and their values measured from the full 6D particle phase space. As expected from Figure 11, we have found no significant dependence on the viewing angle. We show these quantities in Table 2 for the 30 cases studied (3 for each of the 10 haloes). We can see from this Table that, with 40 particles per bin, the virial mass is a little more underestimated, while the concentration parameter is less overestimated and the anisotropy less underestimated. This behaviour of c and β can be understood by recalling that in the case of using only 40 particles per bin the sampling errors of the moments are much larger. For very negative kurtosis small errors may enforce low β estimates, which have to be made up by high c values (to reproduce velocity dispersion). Moreover, we find that the error bars listed in Table 2 are similar in both cases, which indicates that the physical variations due to substructure and to the different shapes of haloes dominate over the statistical noise or sampling errors.

Table 3 shows the statistical significance of the biases on the parameters, using the Student’s t -statistic, which assumes Gaussian distributions of the parameters ($\log M_{100}$, $\log c$, β and σ_r/σ_θ), and the binomial statistic testing the

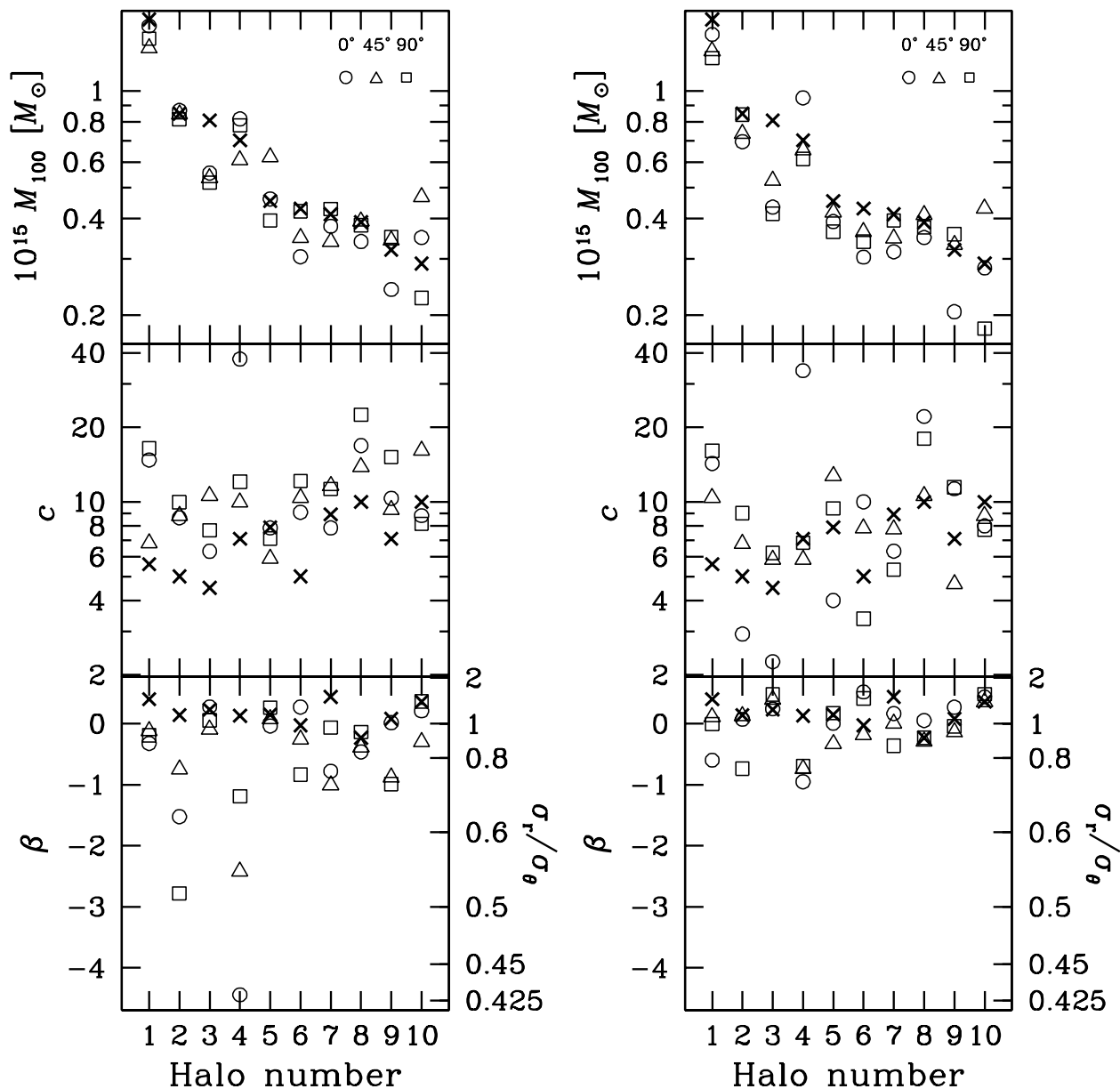


Figure 11. Fitted (on projected data) values of virial mass M_{100} , concentration parameter c and anisotropy β of the ten haloes for the three directions of observation with respect to the major axis of each halo: 0° (circles), 45° (triangles) and 90° (squares). The values measured on 3D data are shown with crosses. *Left:* Fitted parameters obtained with all particles. *Right:* Fitted parameters obtained with 40 particles per bin.

distribution of the signs of these parameters. The two statistical tests lead to different conclusions about the bias of the parameters: the Student's t -statistic always leads to significant biases, while the binomial statistic indicates no significant bias in concentration parameter and velocity anisotropy when only 40 particles are used per radial bin. This difference is caused by the skewed distributions of $\Delta \log c$, $\Delta \beta$ and $\Delta \log(\sigma_r/\sigma_\theta)$. Although the Student's t -statistic has the advantage of being more sensitive to the outliers in the distribution, it has the disadvantage of only being valid for

Gaussian parent distributions, which is not the case here. In summary, in the case of 40 particles per radial bin, while the virial mass is biased towards lower values, we cannot conclude that the concentration parameter and velocity anisotropy are biased with the data we have.

Given the range of $\Delta \log c$ seen in the right plots of Figure 11 (see also Table 2), the discrepancies noted by Lokas & Mamon (2003) between their concentration parameter for Coma and the lower values obtained by Biviano & Girardi (2003) and Biviano et al. (2003) in their

Table 3. Statistical significances in the biases of the fitting procedure

| Particles per bin | $\log M_{100}$ | | $\log c$ | | β | | $\log(\sigma_r/\sigma_\theta)$ | |
|----------------------|----------------|-------|----------|-------|---------|-------|--------------------------------|-------|
| | P_t | P_b | P_t | P_b | P_t | P_b | P_t | P_b |
| All | 0.96 | 0.90 | 1 | 1 | 1 | 1 | 1 | 1 |
| 40 | 1 | 1 | 0.96 | 0.71 | 0.96 | 0.82 | 0.99 | 0.82 |

Notes: P_t and P_b are the probabilities for bias using the Student's t and binomial statistics, respectively.

kinematical analysis of stacked clusters are reduced. Assuming that the departures in $\log c$ are independent of c and M_{100} , we deduce that the difference in $\log c$ between the measurement for the Coma cluster ($c = 9.4$) by Lokas & Mamon and the smaller concentration ($c = 5.5$) found by Biviano et al. can be accounted for in 27% of our 30 projected haloes. On the other hand, the larger difference in $\log c$ between the Coma measurement and the concentration found by Biviano & Girardi (2003) can be accounted for in only 10% of our projected haloes. Similarly, the difference in $\log c$ between Coma and the value ($c = 6$) extrapolated from the values found by Bullock et al. (2001) in their cosmological simulations, can be accounted for in 10 out of our 30 projected haloes. Moreover, there is a non-negligible scatter in the relation between halo concentration and mass (Jing 2000; Bullock et al. 2001), which reduces even more any discrepancy with high concentration found for Coma.

5 DISCUSSION

We studied the dynamical and kinematical properties of dark matter haloes obtained in cosmological N -body simulations. First, using all the 3D information available, we calculated their virial masses, radii, anisotropy parameters and estimated their density profiles. Next, we obtained projected velocity moments, standard observables used to estimate the dark matter content of virialized objects. We then fitted those ‘data’ with spherical models based on Jeans equations in order to reproduce the ‘observed’ velocity moments.

Our approach was similar to the one of Tormen et al. (1997) who used lowest order Jeans equation to model the velocity dispersion and find the masses of simulated haloes and compared them to the real masses of those haloes. In addition to velocity dispersion, we used the projected kurtosis profiles in a similar way to that applied recently by Lokas & Mamon (2003) to infer the properties of the Coma cluster. The use of kurtosis allows us to estimate the anisotropy of the velocity distribution. Besides the virial mass and anisotropy parameter, we fitted the concentration of the density profiles of the haloes.

Our results emphasize the difficulties in the use of higher velocity moments to infer the properties of dark matter haloes. The kurtosis seems to be very sensitive to the substructure and local matter flows. The discrepancies in the fitted properties of halo 4 can be traced to its peculiar mean radial velocity inside the virial radius which amounts to $0.26 v_{100}$, while it is smaller than $0.1 v_{100}$ for most of the remaining haloes (also in the tangential directions). We therefore confirm the necessity of using only elliptical galaxies as tracers in the analysis of single clusters in order to

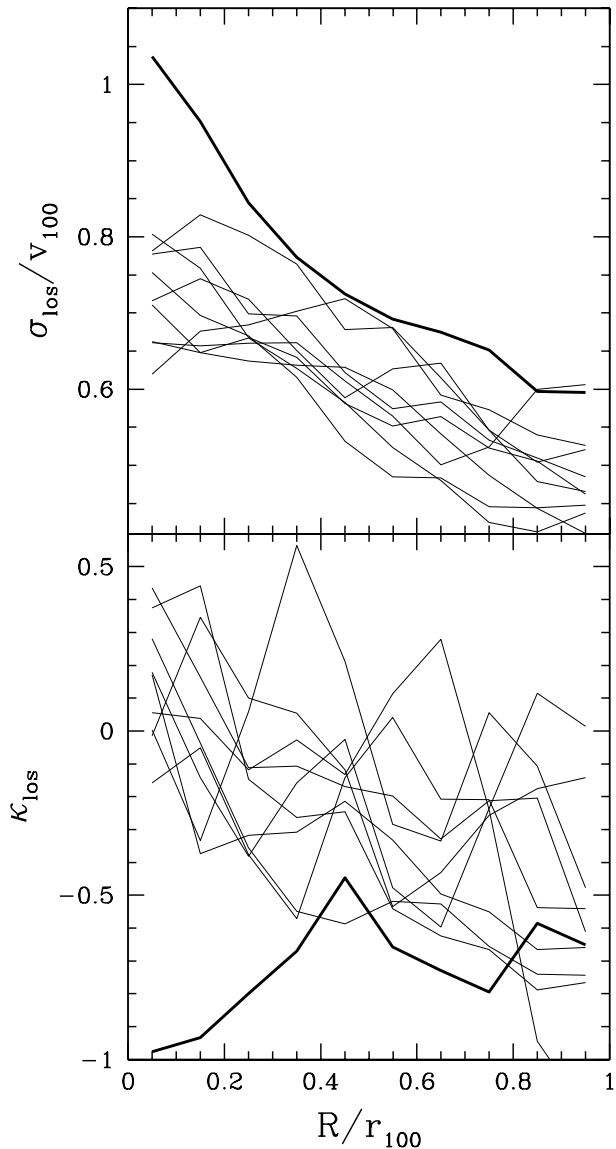


Figure 12. Line-of-sight velocity dispersion (*top*) and kurtosis (*bottom*) vs. projected distance to the centre measured at 0° to the principal axis of the ten most massive haloes in the simulation box. The *thick line* shows the results for halo 4, while the *thin lines* show the other nine haloes.

minimize the effects of infall. Another source of problems lies in our very simple modelling of velocity anisotropy with constant β , while this quantity really shows some radial dependence. Again, in the case of halo 4 this dependence is rather unexpected, departing from isotropy in the very centre of the halo.

In order to check to what extent the rather discrepant results for halo 4 are an exception or commonplace, we show, in Figure 12, the line-of-sight velocity dispersion and kurtosis of the ten most massive haloes in the simulation box for an observer placed along the major axis of each halo. The thick line shows the results for halo 4, while for the rest of the haloes thin lines are used. We infer from Figure 12 that the velocity moments of halo 4 follow an uncharacteristic pattern, probably caused by the unusually large negative

mean radial velocity of this halo (Table 1). We have also checked the pattern of the even velocity moments for the other two directions of observation used in Sections 3 and 4. In these cases, we found that the halo departing most from the general trend was halo 10, which has the highest mean velocity inside the virial radius with respect to v_{100} (with a smaller ratio than halo 4). Therefore, local matter flows, as witnessed by non-zero mean velocity profiles, produce perturbed line-of-sight velocity dispersion and/or kurtosis profiles, which themselves can lead to an inaccurate estimate of the mass, concentration and/or velocity anisotropy of a cluster of galaxies. It is important to note, however, that concentration and anisotropy seem to be more affected than the mass estimation, which is quite robust.

Figure 12 also shows a general trend of the behaviour of the kurtosis of the simulated haloes. We notice that the kurtosis tends to be positive near the centre of the halo and negative at large distances. This means that the velocity distribution is more peaked at the centre and more flattened outside than the purely Gaussian distribution in agreement with a recent finding of Kazantzidis, Magorrian & Moore (2003). But in spite of these departures from Maxwellian velocities at all radii, the Jeans analysis used here and in Lokas & Mamon (2003) produces fairly accurate measurements of the virial mass and concentration parameter (see Fig. 11 and Table 2).

Although obvious interlopers to the haloes have been removed in a similar fashion as in Lokas & Mamon (2003, see also Kent & Gunn 1982), our results could depend on the neighborhood of the analyzed haloes. This would be the case if other haloes with similar velocity were present in the direction of observation, so that their particles would not be removed by the procedure described in Section 3. To estimate the plausibility of such a case, we have calculated for every halo with mass up to one tenth of the mass of the most massive halo in the simulations (that makes a total of 40 haloes) the probability that choosing an observer at a random position around it, there would be one or more perturbing haloes with a mass greater than 25% of the mass of the studied halo, at a projected distance from the halo smaller than r_{100} and with a mean line-of-sight velocity within the interval $[\bar{v}_{10s} - 3v_{100}, \bar{v}_{10s} + 3v_{100}]$, where \bar{v}_{10s} and v_{100} are the mean line-of-sight velocity and circular velocity at r_{100} of the analyzed halo. Choosing randomly 100 observers for each halo, we found that the probability of not finding any perturbing neighbouring halo was higher than 95% for 93% of the haloes, while for two of the analyzed haloes this probability was 88% and only one among the 40 haloes had this probability smaller than 80% (77%). We can conclude from these numbers that it is quite unlikely that the results of the Jeans analysis are affected by neighbouring clusters. Moreover, the least isolated, i.e. the halo with the highest probability of having a perturbing halo around, among the top 10, halo 10, shows no specific bias in the parameter estimates (see Fig. 11).

Therefore, on one hand, the observed cosmic variance of the inner structure and internal kinematics of the massive haloes in the cosmological simulations suggests that the typical properties of dark matter haloes are best obtained through the analysis of stacked observations as performed by Carlberg, Yee & Ellingson (1997), Biviano & Girardi (2003) and Biviano et al. (2003). But, on the other hand, in struc-

tures (clusters of galaxies) with near zero mean velocity profiles, this cosmic variance is much reduced. Therefore, it is well worth analyzing a single cluster with a large number of velocities and a near zero mean velocity, such as was done by Lokas & Mamon (2003) for the Coma cluster.

ACKNOWLEDGMENTS

We wish to thank the anonymous referee for his/her comments and suggestions that helped to improve this paper and E. Salvador-Solé for his comments on the manuscript. We are also indebted to François Bouchet, Bruno Guiderdoni and coworkers for kindly providing us with their N -body simulations, especially Jeremy Blaizot for answering our technical questions about the design and access to the simulations. TS and ELL are grateful for the hospitality of the Institut d’Astrophysique de Paris where part of this work was done. TS and ELL benefited from the Marie Curie Fellowship and the NATO Advanced Fellowship, respectively. ELL and GAM both acknowledge the France-Poland Jume-lage exchange programme. TS and GAM also acknowledge the hospitality of the Copernicus Center in Warsaw where most of this work was performed. Partial support was obtained from the Polish State Committee for Scientific Research within grant No. 2P03D02319. TS acknowledges support from a fellowship of the Ministerio de Educación, Cultura y Deporte of Spain.

REFERENCES

- Binggeli B., 1982, *A&A*, 107, 338
- Binney J., Mamon G. A., 1982, *MNRAS*, 200, 361
- Biviano A., Girardi M., 2003, *ApJ*, 585, 205
- Biviano A., Katgert P., Thomas T., Mazure A., 2003, in Avila-Reese V. et al., eds, *Proc. Cozumel Conference, Galaxy Evolution: Theory and Observations*, *RevMexAA*, in press, astro-ph/0301343
- Bullock J. S., Kolatt T. S., Sigad Y., Somerville R. S., Kravtsov A. V., Klypin A. A., Primack J. R., Dekel A., 2001, *MNRAS*, 321, 559
- Carlberg R. G., Yee H. K. C., Ellingson, E., 1997, *ApJ*, 478, 462
- Cole S., Lacey C., 1996, *MNRAS*, 281, 716
- Davis M., Efstathiou G., Frenk C. S., White S. D. M., 1985, *ApJ*, 292, 371
- Hatton S., Devriendt J. E. G., Ninin S., Bouchet F. R., Guiderdoni B., Vibert D., 2003, *MNRAS*, 343, 75
- Jing Y. P., 2000, *ApJ*, 535, 30
- Jing Y. P., Suto Y., 2002, *ApJ*, 574, 538
- Kazantzidis S., Magorrian J., Moore B., 2003, *ApJ*, in press, astro-ph/0309517
- Kent S. M., Gunn J. E., 1982, *AJ*, 87, 945
- Kitayama T., Suto Y., 1996, *ApJ*, 469, 480
- Lokas E. L., 2002, *MNRAS*, 333, 697
- Lokas E. L., Hoffman Y., 2001, in Spooner N. J. C., Kudryavtsev V., eds, *Proc. 3rd International Workshop, The Identification of Dark Matter*. World Scientific, Singapore, p. 121
- Lokas E. L., Mamon G. A., 2001, *MNRAS*, 321, 155
- Lokas E. L., Mamon G. A., 2003, *MNRAS*, 343, 401

- Merrifield M. R., Kent S. M., 1990, *AJ*, 99, 1548
Merritt D., 1987, *ApJ*, 313, 121
Navarro J. F., Frenk C. S., White S. D. M., 1997, *ApJ*, 490,
493
Tonry J. L., 1983, *ApJ*, 266, 58
Tormen G., Bouchet F. R., White S. D. M., 1997, *MNRAS*,
286, 865
Tully R. B., Shaya E. J., 1984, *ApJ*, 281, 31
van der Marel R. P., Magorrian J., Carlberg R. G., Yee H.
K. C., Ellingson E., 2000, *AJ*, 119, 2038
Wang Q. D., Ulmer M. P., 1997, *MNRAS*, 292, 920